ChemPhotoChem

Research Articles
doi.org/10.1002/cptc.202200192

Chemistry Europe
European Chemical
Societies Publishing

www.chemphotochem.org

Thermally Induced Oxygen Vacancies in BiOCl Nanosheets and Their Impact on Photoelectrochemical Performance**

Xiaofeng Wu,[a, b] Freddy E. Oropeza,[a, c] Daan den Boer,[d] Peter Kleinschmidt,[e] Thomas Hannappel,[e] Dennis G. H. Hetterscheid,[d] Emiel J. M. Hensen,[a] and Jan P. Hofmann*[a, b]

Oxygen vacancies (OVs) have been reported to significantly alter the photocatalytic properties of BiOCl nanosheets. However, their formation mechanism and their role in the enhancement of photoelectrochemical performance remain unclear. In this work, thermally induced oxygen vacancies are introduced in BiOCl nanosheets by annealing in He atmosphere at various temperatures and their formation mechanism is investigated by in-situ diffuse reflectance infrared (DRIFTS) measurements. The influence of OVs on band offset, carrier concentrations and photoelectrochemical performance are systematically studied. The results show that (1) the surface of BiOCl nanosheets is extremely sensitive to temperature and defects are formed at temperatures as low as 200 °C in inert atmosphere. (2) The formation of surface and bulk OVs in BiOCl is identified by a combination of XPS, in-situ DRIFTS, and EPR experiments. (3) The photocurrent of BiOCl is limited by the concentration of charge carriers and shallow defect states induced by bulk oxygen vacancies, while the modulation of these parameters can effectively increase light absorption and carrier concentration leading to an enhancement of photoelectrochemical performance of BiOCl.

Introduction

Bismuth oxychloride (BiOCl), a promising V–VI-VII layered ternary semiconductor, has been widely studied in environmental and energy conversion applications.[1,2] It is a layered structure with $[Bi_2O_2]^{2+}$ slabs interleaved by a double layer of Cl^- ions. Compared to other metal-oxide semiconductors, this unique layered structure produces a built-in electric field and facilitates the separation of photo-generated charge carriers.[3,4] However, the large bandgap (3.4 eV) in the UV range and low quantum efficiency of bulk BiOCl photocatalysts have seriously hampered their photocatalytic application.[5,6]

Up to now, several strategies have been proposed to solve the above-mentioned issues, including non-metal doping, preparation of homojunction and heterojunction composites,[7,8] or metal co-catalyst deposition.[9] Among those strategies, introduction of defects is a simple and efficient way to improve the photocatalytic performance of BiOCl.[5,10] According to the differences in atomic structure, defects can be categorized as point defect, line defects, planar defects and volume defects. The relation between these defects and photocatalytic activity may be complex and elusive. For instance, oxygen vacancies (OVs) in metal oxide semiconductors, considered point defects, can sensitively influence photoelectrochemical properties.[11–13] Recently, the study of surface OVs has emerged as a hot research topic, because most catalytic reactions occur on the surface of catalytic materials and a deep understanding of the nature of surface OVs is needed to design and prepare highly efficient photocatalysts. For example, Li et al. reported that surface OVs in BiOCl can improve water adsorption and reduce activation energy barriers for photocatalytic water oxidation.[14] Zhao et al. discovered that different pathways of molecular oxygen activation are prevailing on (001) and (010) crystal planes of BiOCl nanosheets in the presence of surface OVs.[15]

At the same time, the bulk properties of the semiconductor are equally important in determining the efficiency of a photoelectrochemical reaction. Separation and migration of photo-generated charge carriers first occur in the bulk of the

[a] X. Wu, Dr. F. E. Oropeza, Prof. Dr. E. J. M. Hensen, Prof. Dr. J. P. Hofmann
Laboratory of Inorganic Materials and Catalysis
Department of Chemical Engineering and Chemistry
Eindhoven University of Technology
P.O. Box 513, 5600 MB Eindhoven (The Netherlands)

[b] X. Wu, Prof. Dr. J. P. Hofmann
Surface Science Laboratory, Department of Materials and Earth Sciences
Technical University of Darmstadt, Otto-Berndt-Strasse 3
64287 Darmstadt (Germany)
E-mail: hofmann@surface.tu-darmstadt.de
Homepage: www.mawi.tu-darmstadt.de/of

[c] Dr. F. E. Oropeza
Photoactivated Processes Unit, IMDEA Energy Institute
Parque Tecnológico de Móstoles, Avda. Ramón de la Sagra 3
Móstoles, 28935 Madrid (Spain)

[d] D. den Boer, Dr. D. G. H. Hetterscheid
Leiden Institute of Chemistry, Leiden University
Einsteinweg 55, 2300 RA Leiden (The Netherlands)

[e] Dr. P. Kleinschmidt, Prof. Dr. T. Hannappel
Institute of Physics, Fundamentals of Energy Materials
Technische Universität Ilmenau, Gustav-Kirchhoff-Strasse 5
98693 Ilmenau (Germany)

ChemPhotoChem

Research Articles
doi.org/10.1002/cptc.202200192

Chemistry Europe
European Chemical
Societies Publishing

materials. In addition, bulk modification, such as doping and defects, remarkably affect light harvesting ability and band alignment.[16–18] Nonetheless, bulk defects are commonly regarded as recombination centers for charge carriers, and therefore, unfavorable for photoelectrochemical performance.[19,20] Taking these studies into account, it appears that experimental relationships between the presence of bulk OV defects, shallow or deep defect states in the band gap and the photoelectrochemical performance of OV-rich BiOCl still need to be established.

In this work, BiOCl samples were prepared by a hydrothermal method and OVs were introduced by thermal annealing at different temperatures in inert gas atmosphere. The formation process of OVs is investigated by in-situ diffuse reflectance FT-IR spectroscopy (DRIFTS) experiments. X-ray photoelectron spectra (XPS) show the absence of surface OVs in as-prepared BiOCl samples, while electron paramagnetic resonance (EPR) confirms the presence of (bulk) OVs. The influence of oxygen vacancies on light absorption, carrier concentration and photoelectrochemical response are further investigated and discussed.

Experimental Details

Sample preparation

Preparation of BiOCl nanosheets

BiOCl nanosheets are synthesized by a hydrothermal method according to reference.[21] Briefly, 2 mmol of $Bi(NO_3)_3 \cdot 5H_2O$ (Aldrich, 99.99%) were dissolved in 50 mL of an aqueous D-mannitol (Aldrich, 98%) solution (0.1 mol L^{-1}) followed by 1 hour of agitation. After that, 10 mL of saturated aqueous NaCl (Aldrich, 99%) solution was added dropwise to the above solution under stirring. Subsequently, this mixture was transferred to a 100 mL Teflon-lined autoclave and heated at 160 °C for 3 h. The precipitates were washed with water and ethanol for 7–8 times and then collected after drying at 60 °C for overnight. For simplicity, the as-prepared, pristine sample is denoted as BOC-S0.

Thermal treatment of BiOCl nanosheets

The introduction of oxygen vacancies of BiOCl is conducted at various temperatures in helium atmosphere, the gas flow rate and ramping rate are 50 ml min^{-1} and 5 °C min^{-1}, respectively. The annealing samples are denoted as BOC-H-x (x indicates annealing temperature in °C). In addition, for comparison, BiOCl annealed at 300 °C in oxygen for 12 h is denoted as BOC-O-300.

Materials characterization

Powder X-ray diffraction pattern were recorded on a Bruker D2 PHASER diffractometer using Cu Kα radiation at a scan rate of 0.02° min^{-1}. BET specific surface area and pore volume were measured on a Tristar 3000 automated gas adsorption system. Transmission electron microscopy (FEI Tecnai 20) was used to observe the morphology and bulk structure of the materials. UV-vis diffuse reflection spectra of BiOCl samples were obtained on a UV-Vis spectrometer (Shimadzu UV-2401, Japan) with $BaSO_4$ as reference. X-ray photoelectron spectra were collected on a Thermo

Scientific K-Alpha spectrometer equipped with a monochromic Al K$_\alpha$ X-ray source (hν = 1486.7 eV). The powder samples were mounted on adhesive double-sided conductive carbon tape on substrate or filled into the holes of a homemade Cu powder sample holder. A low energy electron/ion flood gun neutralizer was used to compensate the surface charging. High resolution spectra of Bi, O and Cl elements were averagely scanned for 30 times and their pass energy was set to 50 eV. Spectra were binding energy calibrated by setting the main line of Bi 4f$_{7/2}$ spectrum to 159.4 eV. All XPS spectra were analyzed and processed by CasaXPS and Origin softwares. EPR spectra were measured on a Bruker EMXplus X-band spectrometer at room temperature in air at a frequency of 9.460–9.470 GHz in 4 mm thin wall quartz glass EPR tubes (Wilmad).

In-situ temperature-controlled diffuse reflectance infrared Fourier transform spectroscopy (DRIFTS) was used to assess surface oxygen vacancy formation. Steady state IR spectra were recorded in the region of 400 to 3950 cm^{-1} at a resolution of 2 cm^{-1} on a Bruker Vertex 70v spectrometer with a room temperature DTGS detector. Pristine BOC-S0 was used as starting sample and heated at 200 °C, 250 °C, and 300 °C in vacuum, respectively. For the oxidation process, dry O_2 (≥ 99.95%) was introduced into the cell at a flow rate of 2 cm^3 min^{-1} at 400 °C for 6 h to oxidize defective BiOCl while the static pressure of the cell was 10 mbar. After cooling down to 298 K, DRIFTS spectra were collected in static vacuum (1 mbar). Dry KBr powder was used as the reference.

Photoelectrochemical measurements were carried out in three-electrode configuration (cIMPS workstation, Zahner-Elektrik GmbH & Co. KG, Germany). 0.1 M sodium phosphate buffer solution containing 0.1 M sodium sulfite was used as electrolyte for photo-current and electrochemical impedance spectroscopy (EIS) measurements. The circular irradiation area was 0.283 cm^2 and the intensity of simulated solar LED white light source was 100 mW cm^{-2}. EIS measurements were conducted in the frequency range between 0.1 Hz and 10 KHz with a perturbation amplitude of 10 mV at open circuit potential (OCP). Mott-Schottky plots were measured at a frequency of 500 Hz in 0.5 M Na_2SO_4 solution in three-electrode configuration. Ag/AgCl (3 M NaCl) and Pt wire were used reference and counter electrodes, respectively and the potential of the Ag/AgCl reference electrode was + 0.251 V.

Working electrodes were prepared on FTO glass (Solaronix, TCO10-10, 10 ohm/sq.) by drop casting. In detail, for pre-treatment, all BiOCl samples were sieved with an 80 μm sieve plate and the smaller particles were kept for further preparation of working electrodes. FTO glass substrates were initially subsequently ultrasonicated in distilled water, ethanol and acetone for 30 minutes each, followed by UV-ozone cleaning treatment for 20 minutes. After that, 100 mg of the above samples were dispersed in a mixed solution of 5 w/w% Nafion^{TM} solution (200 μL) and ethanol (2 mL). Then, the solution was ultra-sonicated for 30 minutes to obtain a uniform white slurry. 100 μL of slurry was carefully dropped and spread out on the FTO substrates (2×2 cm^2). Thin films are formed after natural evaporation of ethanol.

Results and Discussion

Effect of annealing treatment on crystal structure, morphology, and specific surface area

The XRD pattern of BiOCl samples are shown in Figure 1. X-ray diffraction peaks of all BiOCl samples are in accordance with tetragonal phase BiOCl (JCPDS card no. 06-0249). When increas-
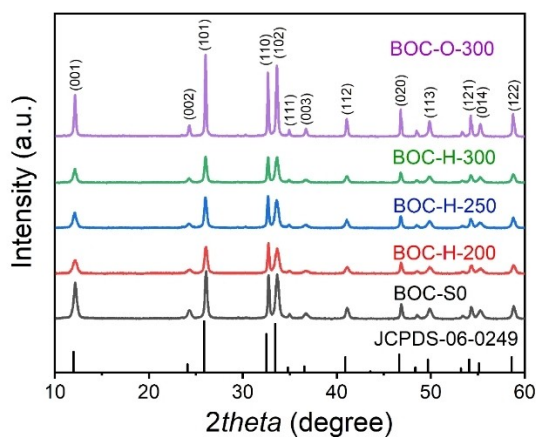
ChemPhotoChem

Research Articles
doi.org/10.1002/cptc.202200192

**Chemistry
Europe**
European Chemical
Societies Publishing

Figure 1. XRD pattern of as-prepared samples with BiOCl JCPDS-06-0249 as reference.
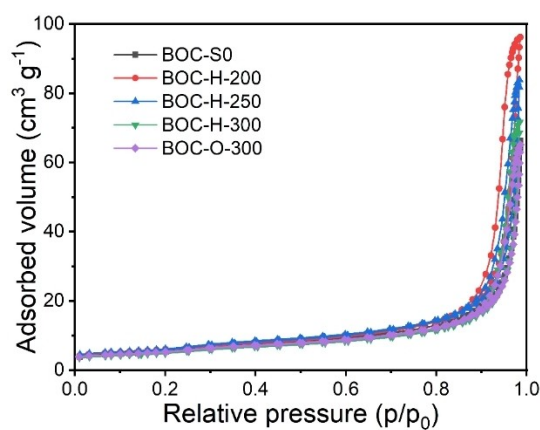

Figure 2. N$_2$ physisorption isotherms of as-prepared samples.

Table 1. Physical properties of the as-prepared BiOCl samples.

Sample	S_{BET} area [m^2 g^{-1}]	Pore volume [cm^3 g^{-1}][a]	Relative crystallinity[b] (001)	(020)	Average crystallite size [nm][c]
BOC-S0	19.5 ($\pm$0.03)	0.11 ($\pm$0.005)	1.00	1.00	23 ($\pm$1)
BOC-H-200	21.2 ($\pm$0.05)	0.15 ($\pm$0.002)	0.58 ($\pm$0.01)	0.73 ($\pm$0.01)	17 ($\pm$1)
BOC-H-250	21.4 ($\pm$0.02)	0.13 ($\pm$0.003)	0.65 ($\pm$0.01)	0.80 ($\pm$0.01)	20 ($\pm$1)
BOC-H-300	17.5 ($\pm$0.01)	0.11 ($\pm$0.004)	0.55 ($\pm$0.01)	0.70 ($\pm$0.01)	23 ($\pm$1)
BOC-O-300	18.7 ($\pm$0.04)	0.10 ($\pm$0.003)	1.68 ($\pm$0.01)	1.72 ($\pm$0.01)	39 ($\pm$1)

[a] Pore volume. [b] Relative crystallinity calculated from the relative intensity of the (001) and (020) diffraction peaks with BOC-S0 as reference. [c] Average crystallite size calculated from Scherrer formula.

ing temperature to 300 °C in helium or oxygen, all BiOCl samples retain their original tetragonal crystal structure, with no obvious diffraction peaks of Bi metal are observed. This indicates that annealing in either O$_2$ or He atmospheres did not significantly change the crystal structure of BiOCl samples. In addition, the annealing process has little effect on the average crystallite sizes of BiOCl samples as estimated via the Scherrer formula (Table 1). However, intensities of the diffraction peaks of BiOCl nanosheets obviously have changed. Using the intensity of the (001) crystal plane as reference, relative crystallinity of BiOCl noticeably increased from 1.00 to 1.68 after annealing in oxygen while it decreased from 1.00 to 0.58, 0.65, 0.55 at 200 °C, 250 °C, 300 °C in helium, respectively (Table 1). Intensity of the (020) crystal facet follows the same trend. These changes are possibly caused by the increasing number of defects during annealing in He.

Additionally, N$_2$ physisorption isotherms of the BiOCl samples were collected to calculate specific surface areas and pore volume (Figure 2). The BET surface area of BOC-S0 is 19.53 m^2 g^{-1} and its pore volume is 0.11 cm^{-2} g^{-1}. These values show a negligible change after treatment at various temperatures in helium and oxygen. The data of physical properties are summarized in Table 1.

From TEM images of BOC-S0 and BOC-H-300 (Figure 3), it can be observed that BOC-S0 shows nanosheet morphology with length and thickness of approximately 100–200 nm and 20–30 nm, respectively. The lattice spacing is 0.730 nm, which implies their exposed (001) crystal facets. After annealing at
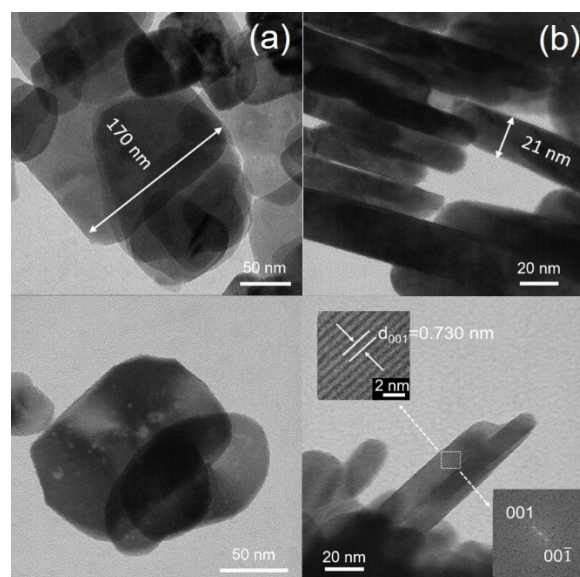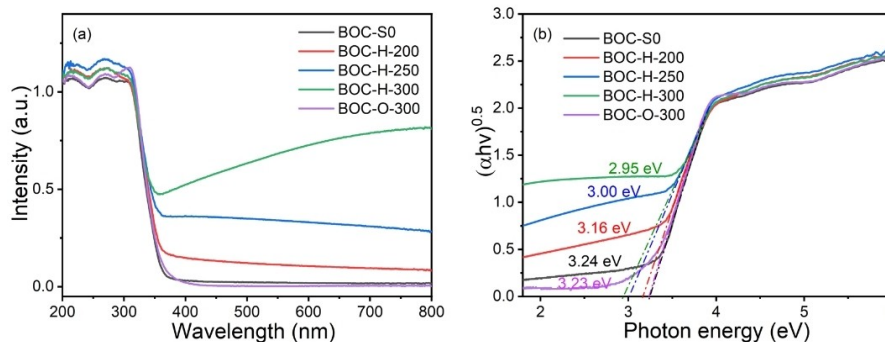

Figure 3. TEM images of BOC-S0 ((a) and (b)) and BOC-H-300 ((c) and (d)).

300 °C in helium, some defects emerged on the (001) crystal facets (Figure 3c, d). Taken together, the above data reflect that annealing in He atmosphere does not significantly change crystal structure, morphology, or porosity of BiOCl nanosheets.

ChemPhotoChem

Research Articles
doi.org/10.1002/cptc.202200192

Chemistry Europe
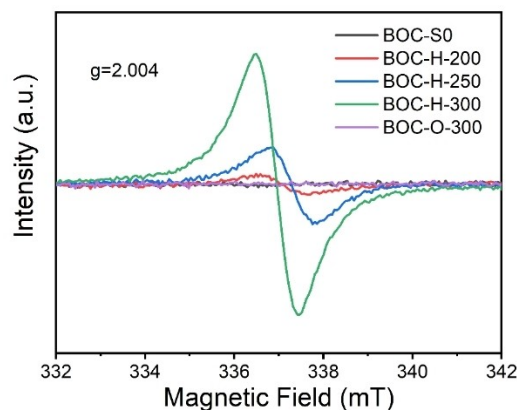European Chemical
Societies Publishing

Light absorption and formation of oxygen vacancies

In order to obtain information about the influence of defects on the optical absorption, UV-Vis diffuse reflectance spectra of the BiOCl samples were recorded. As shown in Figure 4, the absorption edge of BOC-S0 is at about 380 nm and the indirect bandgap calculated from corresponding the Tauc plot is 3.24 eV. The apparent bandgaps for the samples BOC-H-X (200, 250, 300) are 3.16, 3.00, and 2.95 eV, respectively, and decrease with increasing annealing temperature. The reduced bandgap is caused by band tailing due to the presence of a high number of defect states.[22] Interestingly, the bandgap of sample BiOCl-O-300 is restored to the value of the sample BOC-S0, indicating the healing of OV defects by O_2 annealing treatment. UV-Vis spectra of BOC-H-X (200, 250, 300) show a large increase of light absorption in the visible light range, while BOC-O-300 shows no changes. This extended light absorption at longer wavelengths has been reported to originate from oxygen vacancies.[23,24] EPR spectra were measured to verify the presence of OVs (Figure 5). A significant peak appears positioned at $g = 2.004$, which is the typical signature for trapped electrons in OVs.[10] With an increasing annealing temperature in helium atmosphere, the respective signal gradually becomes larger, indicating an increasing amount of OVs. Consistently, BOC-O-300 shows no response in the EPR spectra which relates to the absence of OVs after annealing in oxygen. In comparison to other reducible oxides, BiOCl is much more sensitive and prone to form OVs at low temperature. For instance, TiO_2 starts to be reduced at 500 °C during H_2-TPR measurements.[25] Surface and bulk oxygen of pristine CeO_2 can be removed under H_2 gas atmosphere at 470 °C and 730 °C, respectively.[26] BiOCl is much less stable and phase change occurs at above 400 °C.[27] The readiness to form OVs relates to the low Bi–O bond enthalpy.[2]

XPS measurements have been employed to characterize OVs at the surface of semiconductors.[28,29] The relative content of oxygen vacancies can be extracted from the O 1s and the corresponding metal high resolution core level XP spectra. For instance, it is possible to indirectly obtain the content of OVs through calculating the ratio of Ce^{3+}/Ce^{4+} in the Ce 3d spectrum or the relative area of $O–Ce^{3+}$ in O 1s spectrum.[30]

Figure 5. EPR spectra of BiOCl nanosheets, measured in the dark at 298 K.

However, XPS is very surface sensitive with an information depth of few nanometers, depending on photoelectron kinetic energy. In our case, high resolution XP spectra of Bi 4f, O 1s and Cl 2p regions remain almost unchanged with the different treatments indicating the absence of surface OVs (Figure 6a, Figure 6b and Figure 6c). No changes are observed in valence band XPS. The absence of spectral features between VBM and E_F indicates that there are no occupied defect states in the band gap close to the VBM (Figure 6d). The XPS and EPR results taken together with the reported high reactivity of surface OVs in BiOCl,[9] let us presume that surface OVs formed by annealing in He have been quickly replenished by subsequent exposure to ambient air during sample handling and preparation and that the OVs seen by EPR are located mainly in the bulk of the materials.[31]

Photoluminescence (PL) is commonly used to determine the energy positions of defect states in the band gap and evaluate separation efficiency of photogenerated charge carriers.[32] The range of PL spectral features associated with OVs-created defect states is relative wide. The PL spectra of the BiOCl samples taken at room temperature show a broad distribution of PL intensity in the range of 340–500 nm (Figure 7). The distinct peak at 423 nm is associated with a defect state 2.93 eV above valence band maximum (denoted as
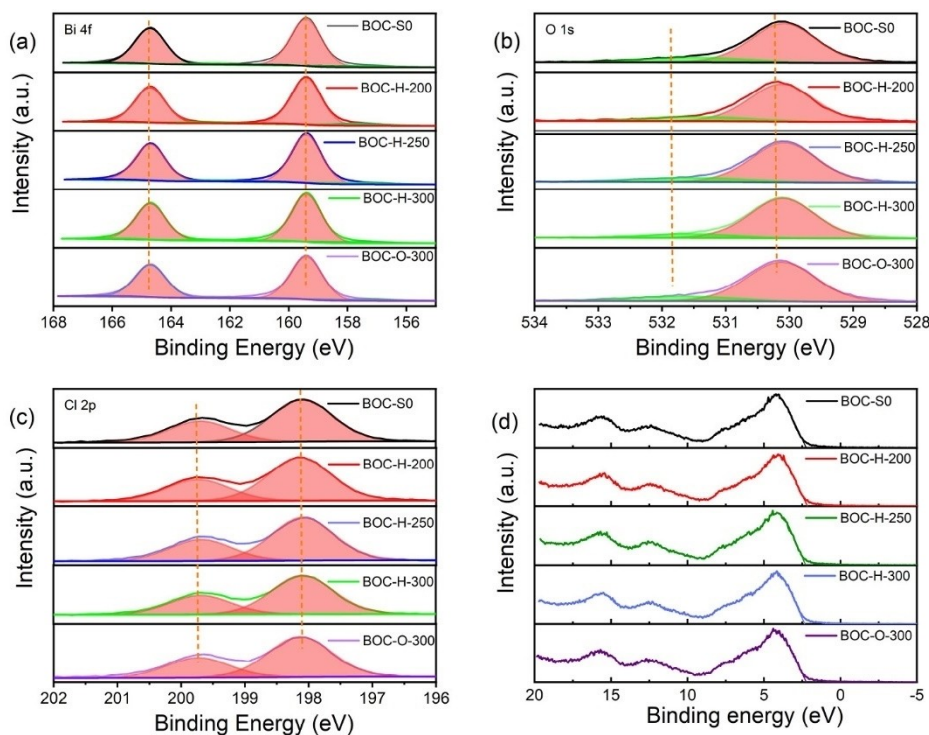

Figure 4. UV-Vis diffuse reflectance spectra (a) and the corresponding Tauc plots (b) of as-prepared and differently treated BiOCl samples. An indirect bandgap is assumed, according to literature.[3,21]

Figure 6. Bi 4f (a), O 1s (b), Cl 2p (c) high resolution XP spectra and X-ray valence band spectra (d) of as-prepared BiOCl samples.

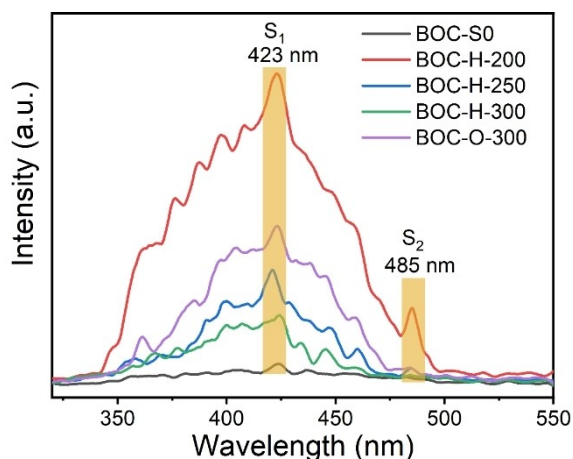**Figure 7.** Photoluminescence spectra of BiOCl samples, measured at room temperature.

Figure 8. Defect state positions of BiOCl samples, calculated from bandgap and photoluminescence spectra.

S_1 in Figure 8) and corresponds to the main recombination process of charge carriers. The required excitation energy of electrons trapped at S_1 in BOC-H-250 sample is only 0.070 eV ($= E_{CBM} - E_{S1}$), which is close to 3 kT (0.078 eV). This means that the trapped electrons can be excited thermally at 298 K. Therefore, S_1 states are not regarded as effective recombination centers for BOC-H-250 and BOC-H-300 samples. However, this excitation energy reaches up to 0.23 eV in BOC-H-200, which makes it less likely that trapped electrons get thermally excited at 298 K. In this sample, additionally, a new deep defect state (denoted as S_2) at 2.56 eV (485 nm) above VBM emerged. These t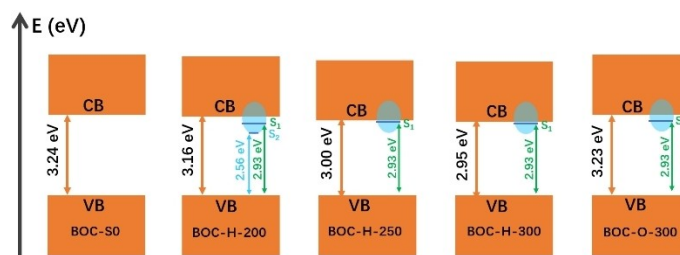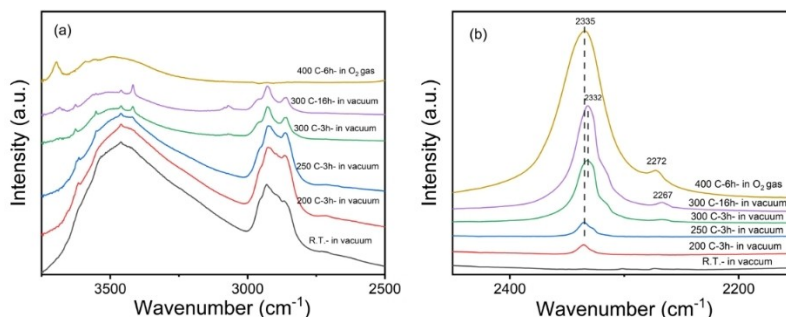wo recombination centers re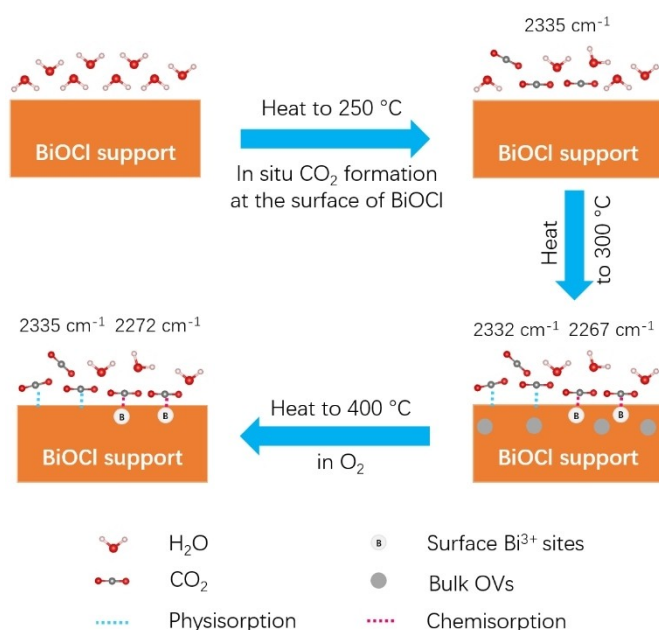lated to defect states contribute to the high photoluminescence intensity for BOC-H-200 sample (Figure 8). The amount of S_2 will decrease or even disappear with increasing annealing temperature.

To investigate the mechanism of thermally induced OV formation, in-situ DRIFTS experiments on BOC-S0 were conducted at various temperatures and a pressure <1 mbar. As shown in Figure 9, a peak centered at 2335 cm^{-1} appeared at 200 °C, which can be ascribed to physisorbed CO_2 after thermal removal of water. The amount of physisorbed CO_2 obviously increases as the amount of adsorbed water decreases. When the temperature increased to 300 °C, CO_2 physisorption became stronger and a noticeable red shift is observed from 2335 cm^{-1} to 2332 cm^{-1}. This change originates from influence of an increased amount of bulk OVs. Meanwhile, a small peak at 2267 cm^{-1} emerged, which can be ascribed to CO_2 chemisorption on Bi^{3+} at the surface of defective BiOCl.[33] Interestingly, these two peaks shift back to their original positions after oxygen treatment at 300 °C for 16 h. This is possibly because
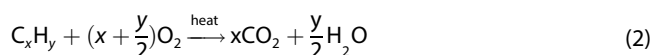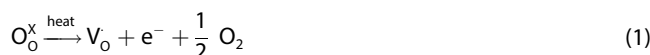
ChemPhotoChem

Research Articles
doi.org/10.1002/cptc.202200192

Chemistry Europe
European Chemical
Societies Publishing

Figure 9. *In-situ* DRIFTS of pristine BOC-S0 sample in the range of 2500–3750 cm^{-1} (a) and 2150–2450 cm^{-1}, measured in static vacuum (< 1 mbar) at 298 K.
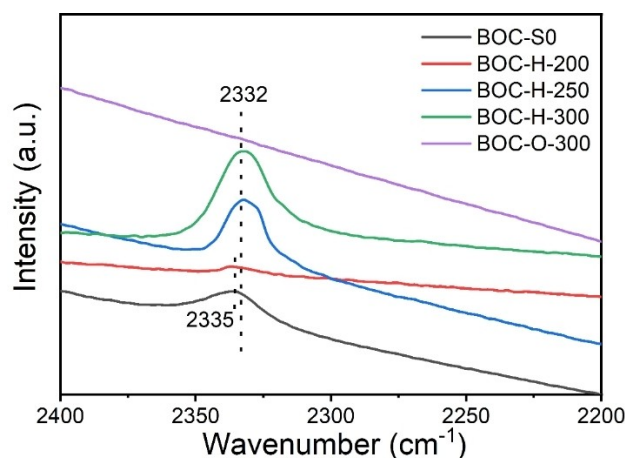
most of bulk OVs are healed and lead to reduction of the binding strength of CO_2 molecules at the surface. The CO_2 adsorption process can be understood as depicted in Figure 10. We anticipate residues of the D-mannitol from synthesis as well as other adventitious carbon species reacting with lattice oxygen of BiOCl as the source for CO_2 in the DRIFTS experiments. This viewpoint is confirmed by the decrease of hydrocarbon related absorption features between 3000–2800 cm^{-1} (C−H stretching region) upon increasing temperature. Moreover, D-mannitol starts to decompose when the temperature increases above 300 °C according to literature.[34] The formation and recovery process of bulk OVs can be described in Kröger-Vink notation as follows. Firstly, bulk OVs are formed in BiOCl samples and O_2 is released at low temperature (Eq. 1). Secondly, D-mannitol or adventitious carbon decomposition to produce CO_2 and water and physisorption occurs at the surface of BiOCl (Eq. 2), followed by CO_2 chemisorption on surface Bi^{3+} sites when increasing temperature to 300 °C. Finally, bulk OVs are healed by O_2 introduction at 400 °C (Eq. 3).

$$O_O^x \xrightarrow{heat} V_O^{\cdot} + e^- + \frac{1}{2} O_2 \tag{1}$$

$$C_xH_y + (x + \frac{y}{2})O_2 \xrightarrow{heat} xCO_2 + \frac{y}{2}H_2O \tag{2}$$

$$V_O^{\cdot} + e^- + \frac{1}{2} O_2 \rightarrow O_O^x \tag{3}$$

As elaborated above, the OVs of the temperature treated BiOCl samples are located in the bulk rather than at the surface. To further confirm this point, we also measured transmission FTIR spectra of all BiOCl samples pressed into KBr pellets in the evacuated sample compartment of the FTIR spectrometer at reduced pressure of < 5 mbar at 298 K (Figure 11). The peak at 2332 cm^{-1} results from CO_2 physisorption from the residual gas.[35] Interestingly, there are no indications of CO_2 chemisorption in the region of 2260–2270 cm^{-1}, although that would have been expected for defective BiOCl.[33] The high reactivity of surface OVs towards atmospheric oxygen leads to their facile replenishment when in contact to air. Consistently, Zhang et al. reported that surface OVs in BiOCl basically disappeared after repeated use in benzyl alcohol oxidation for 5 times, which implies that surface OVs of BiOCl are highly reactive.[9]

Figure 10. Proposed schematic mechanism of BiOCl OVs formation based on *in-situ* DRIFTS results in Figure 9.

Figure 11. Transmission FTIR spectra of BiOCl samples, measured as KBr pellets in static vacuum at 298 K.

ChemPhotoChem

Research Articles
doi.org/10.1002/cptc.202200192

**Chemistry
Europe**
European Chemical
Societies Publishing

Effect of bulk oxygen vacancies on photoelectrochemical performance

To investigate the effect of bulk OVs on the photoelectrochemical performance of BiOCl samples, chopped light voltammetry measurements on BiOCl/FTO glass photoelectrodes were carried out. In spite of similar specific surface areas and morphologies, the differently treated BiOCl materials show remarkably different photocurrents at open circuit potential (Figure 12a). Photocurrents under irradiation for all samples annealed in He are significantly higher than that of the as-prepared sample, reaching up to 1.17 µA cm^{-2} for BOC-H-300, which is 7 times higher than that of BiOCl (0.13 µA cm^{-2}). In contrast, O$_2$-annealing seems to be detrimental as the photocurrent for sample BOC-O-300 drops to 0.08 µA cm^{-2}. The maximum theoretically achievable photocurrent density of BiOCl (3.2 eV) is around 500 µA cm^{-2} under 100 mW cm^{-2} simulated solar light illumination.[36] However, the practical photocurrent will strongly be limited by light absorption, separation and transport of charge carriers as well as the rate of the surface redox reactions.[37] Although bulk defects may act as recombination centers for photogenerated charge carriers and are thus unfavorable for photoelectrochemical activity,[20] the overall effect of OVs formation on PEC performance is positive. Moreover, an enhancement of crystallinity in sample BOC-O-300 is not beneficial to the photoelectrochemical properties. A high crystallinity may accelerate the separation and migration of charge carriers. However, this effect seems not to outweigh the depletion of O vacancies defects in these samples, suggesting that carrier mobility in BiOCl is not the rate-limiting step for the photoelectrochemical performance.

For driving the photoelectrochemical process, the charge carriers need to pass through the space charge region and the electrochemical double layer at the semiconductor solution junction. Electrochemical impedance spectroscopy (EIS) is capable to determine resistances and capacities in the semiconductor solution interface by fitting equivalent circuits. In our study, EIS was conducted at open circuit potential (OCP) in the dark. The BiOCl electrolyte interface can be fit in first approximation by a Randles equivalent circuit, describing charge transfer and diffusion processes (Figure 12b). The smaller the diameters of the semicircles of the plots, the smaller is the charge transfer resistance and the higher is the charge transfer rate at the interface. Compared to BOC-S0, defective BiOCl samples, i.e., BOC-H-200, BOC-H-250, BOC-H-300 qualitatively possess smaller charge transfer resistances.

Mott-Schottky plots were recorded to determine band alignment and concentrations of charge carriers in the different BiOCl samples (Figure 13). The slopes of the Mott-Schottky plots are positive, indicating n-type behavior, consistent with literature.[38–40] The open circuit potential (OCP) and flat band position (E_{fb}) were measured and are summarized in Table 2. The band bending (U_{bb}) of BiOCl samples was calculated according to the formula: $U_{bb} = OCP - E_{fb}$.[41] The larger upwards band bending results in a larger contact potential difference at the semiconductor-solution interface. In addition, the donor density can be estimated by the slope of the Mott-Schottky plot according to Equation 4:

$$N_D = \frac{2}{e\varepsilon_0\varepsilon_r \cdot slope \cdot A^2}$$

(4)
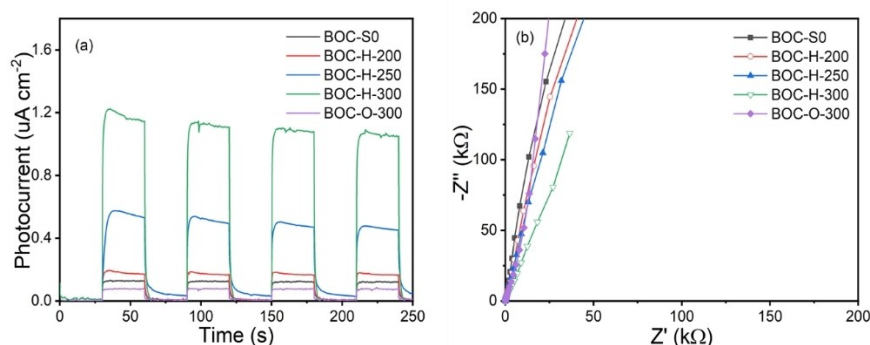
Figure 12. Photocurrent density under 100 mW cm^{-2} white LED light illumination (a) and electrochemical impedance spectroscopy in the dark (b) of as-prepared samples measured in 0.1 M sodium phosphate buffer solution containing 0.1 M Na$_2$SO$_3$, both at open circuit potential.

Table 2. Open circuit potential (OCP) values, energy positions of flat band (E_{fb}) and band bending (U_{bb}), the slopes of Mott-Schottky plots and calculated corresponding concentrations of charge carriers measured in 0.5 M Na$_2$SO$_4$ solution at 298 K. Error indicators in brackets.

Sample	OCP [V vs. RHE]	E_{fb} [V vs. RHE]	$U_{bb}=$ OCP$-E_{fb}$	Slope [10^{10} F^{-2}V^{-1}]	Concentration of charge carriers [cm^{-3}]
BOC-S0	0.93 ($\pm$0.01)	−0.12 ($\pm$0.02)	1.05 ($\pm$0.03)	18.5 ($\pm$0.2)	2.88($\pm$0.03)$\times10^{16}$
BOC-H-200	0.86 ($\pm$0.04)	−0.12 ($\pm$0.04)	0.98 ($\pm$0.08)	4.09 ($\pm$0.1)	1.10($\pm$0.03)$\times10^{17}$
BOC-H-250	1.00 ($\pm$0.01)	−0.22 ($\pm$0.02)	1.22 ($\pm$0.03)	11.7 ($\pm$0.1)	3.78($\pm$0.03)$\times10^{16}$
BOC-H-300	0.93 ($\pm$0.05)	−0.33 ($\pm$0.03)	1.26 ($\pm$0.08)	12.7 ($\pm$0.1)	5.20($\pm$0.04)$\times10^{16}$
BOC-O-300	1.02 ($\pm$0.02)	0.00 ($\pm$0.04)	1.02 ($\pm$0.06)	40.2 ($\pm$0.1)	1.44($\pm$0.004)$\times10^{16}$

ChemPhotoChem

Research Articles
doi.org/10.1002/cptc.202200192

Chemistry Europe
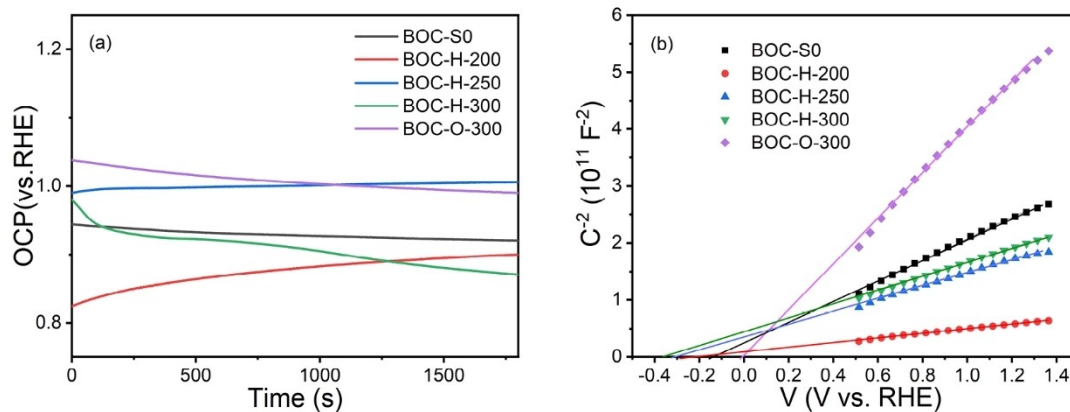European Chemical
Societies Publishing

Figure 13. Open circuit potentials (a) and Mott-Schottky plots (b) of BiOCl samples.

Obviously, BOC-H-200 sample possesses the highest donor density (1.1×10^{17} cm^{-3}) but does not show the highest photocurrent due to severe bulk recombination which is confirmed by photoluminescence measurements. The donor density of BOC-H-300 (5.20×10^{16} cm^{-3}) is 1.8 times and 3.6 times higher than that of BOC-S0 (2.88×10^{16} cm^{-3}) and BOC-O-300 (1.44×10^{16} cm^{-3}), respectively. Except for BOC-H-200, the photocurrent is proportional to the concentration of charge carriers, which reflects that both of defects and concentration of charge carriers affect the photocurrent density.

The conductivity (σ) of semiconductors is determined by mobility (μ) and concentration (n) of charge carriers according to Equation (5):

$$\sigma = nq\mu \tag{5}$$

with q being the elementary charge.

In this sense, OV related deep defect states as recombination centers are unfavorable to transfer charge carriers, because of their impact on the mobility of charge carriers. However, a moderate amount of shallow defect states from which electrons can easily be excited to the conduction band at room temperature does not only increase the concentration but also the separation efficiency of photogenerated charge carriers. Taking into account the layered structure of BiOCl, the distance of $[Bi_2O_2]^{2+}$ and adjacent Cl$^-$ ion layers is relatively large, which gives rise to weak interaction and high energy barrier for charge carriers migration perpendicular to the sheets. We also can look at this from the point of mobility of charge carriers. According to literature,[42] effective masses of holes along x, y, z direction in BiOCl are 0.95 m$_0$, 0.95 m$_0$ and 6.31 m$_0$, respectively, while effective masses of electrons along x, y, z direction are 0.29 m$_0$, 0.29 m$_0$ and 1.15 m$_0$, respectively. Charge carrier mobility of semiconductors is inversely proportional to their effective mass. Therefore, charge carriers show low mobility in z direction. This phenomenon is also found in other 2D layered semiconductors.[43]

Conclusions

In summary, the surface of BiOCl is extremely sensitive to temperature and OVs are formed at temperatures as low as 200 °C in inert atmosphere. In-situ DRIFTS results demonstrate that CO_2 can specifically adsorb on the surface of BiOCl nanosheets bearing OVs and the formation process of OVs could be traced by using CO_2 as IR probe molecule. Introduction of OVs not only increases concentration of charge carriers but also gives rise to two kinds of shallow and deep defect states. Shallow defect states as electrons sinks accelerate separation of charge carriers and remarkably enhance the photocurrent, while deep defect states as recombination centers negatively impact on photocurrent. Finally, photo-electrochemical performance of BiOCl nanosheets is dominantly determined by the balance of OV induced generation (doping) and defect mediated recombination of charge carriers. This work sheds light on the important role of bulk defects in influencing the photo(electro)chemical performance of layered inorganic semiconductors.

Acknowledgements

Conflict of Interest

The authors declare no conflict of interest.

Data Availability Statement

The data that support the findings of this study are available from the corresponding author upon reasonable request.

[1] J. Li, H. Li, G. Zhan, L. Zhang, *Acc. Chem. Res.* **2017**, *50*, 112–121.
[2] H. Li, J. Li, Z. Ai, F. Jia, L. Zhang, *Angew. Chem. Int. Ed.* **2018**, *57*, 122–138; *Angew. Chem.* **2018**, *130*, 128–145.
[3] J. Jiang, K. Zhao, X. Xiao, L. Zhang, *J. Am. Chem. Soc.* **2012**, *134*, 4473–4476.
[4] H. Li, L. Zhang, *Curr. Opin. Green Sustain. Chem.* **2017**, *6*, 48–56.
[5] L. Wang, D. Lv, F. Dong, X. Wu, N. Cheng, J. Scott, X. Xu, W. Hao, Y. Du, *ACS Sustainable Chem. Eng.* **2019**, *7*, 3010–3017.
[6] J. Sun, J. Wu, S.-Z. Yang, Q. Li, J. Xiong, Z. Yang, L. Gu, X. Zhang, L. Sun, *Appl. Catal. B* **2018**, *221*, 467–472.
[7] S. Weng, Z. Fang, Z. Wang, Z. Zheng, W. Feng, P. Liu, *ACS Appl. Mater. Interfaces* **2014**, *6*, 18423–18428.
[8] A. K. Chakraborty, S. B. Rawal, S. Y. Han, S. Y. Chai, W. I. Lee, *Appl. Catal. A* **2011**, *407*, 217–223.
[9] H. Li, F. Qin, Z. Yang, X. Cui, J. Wang, L. Zhang, *J. Am. Chem. Soc.* **2017**, *139*, 3513–3521.
[10] H. Li, J. Shi, K. Zhao, L. Zhang, *Nanoscale* **2014**, *6*, 14168–14173.
[11] S. Niu, R. Zhang, C. Guo, *Mater. Chem. Front.* **2020**, *4*, 2314–2324.
[12] Z. Yang, Y. Shi, H. Li, C. Mao, X. Wang, X. Liu, X. Liu, L. Zhang, *Environ. Sci. Technol.* **2022**, *56*, 3587–3595.
[13] N. Zhang, L. Li, Q. Shao, T. Zhu, X. Huang, X. Xiao, *ACS Appl. Energ. Mater.* **2019**, *2*, 8394–8398.
[14] H. Li, J. Shang, H. Zhu, Z. Yang, Z. Ai, L. Zhang, *ACS Catal.* **2016**, *6*, 8276–8285.
[15] K. Zhao, L. Zhang, J. Wang, Q. Li, W. He, J. J. Yin, *J. Am. Chem. Soc.* **2013**, *135*, 15750–15753.
[16] Y. Yang, L. C. Yin, Y. Gong, P. Niu, J. Q. Wang, L. Gu, X. Chen, G. Liu, L. Wang, H. M. Cheng, *Adv. Mater.* **2018**, *30*, 1704479.
[17] F. Wang, W. Septina, A. Chemseddine, F. F. Abdi, D. Friedrich, P. Bogdanoff, R. van de Krol, S. D. Tilley, S. P. Berglund, *J. Am. Chem. Soc.* **2017**, *139*, 15094–15103.
[18] G. Liu, J. Pan, L. C. Yin, J. T. S. Irvine, F. Li, J. Tan, P. Wormald, H. M. Cheng, *Adv. Funct. Mater.* **2012**, *22*, 3233–3238.
[19] M. Kong, Y. Li, X. Chen, T. Tian, P. Fang, F. Zheng, X. Zhao, *J. Am. Chem. Soc.* **2011**, *133*, 16414–16417.
[20] Y. Zhu, Q. Ling, Y. Liu, H. Wang, Y. Zhu, *Appl. Catal. B* **2016**, *187*, 204–211.
[21] M. Guan, C. Xiao, J. Zhang, S. Fan, R. An, Q. Cheng, J. Xie, M. Zhou, B. Ye, Y. Xie, *J. Am. Chem. Soc.* **2013**, *135*, 10411–10417.
[22] H. J. Yu, R. Shi, Y. X. Zhao, T. Bian, Y. F. Zhao, C. Zhou, G. I. N. Waterhouse, L. Z. Wu, C. H. Tung, T. R. Zhang, *Adv. Mater.* **2017**, *30*, 1605148.
[23] Z. Ma, P. Li, L. Ye, Y. Zhou, F. Su, C. Ding, H. Xie, Y. Bai, P. K. Wong, *J. Mater. Chem. A* **2017**, *5*, 24995–25004.
[24] S. Wu, J. Xiong, J. Sun, Z. D. Hood, W. Zeng, Z. Yang, L. Gu, X. Zhang, S. Z. Yang, *ACS Appl. Mater. Interfaces* **2017**, *9*, 16620–16626.
[25] J. Li, G. Lu, G. Wu, D. Mao, Y. Guo, Y. Wang, Y. Guo, *Catal. Sci. Technol.* **2014**, *4*, 1268–1275.
[26] I. Popescu, I. C. Marcu, *Phys. Chem. Chem. Phys.* **2021**, *23*, 5897–5907.
[27] X. Liu, Y. Su, Q. Zhao, C. Du, Z. Liu, *Sci. Rep.* **2016**, *6*, 28689.
[28] J. Wan, W. Chen, C. Jia, L. Zheng, J. Dong, X. Zheng, Y. Wang, W. Yan, C. Chen, Q. Peng, D. Wang, Y. Li, *Adv. Mater.* **2018**, *30*, 1705369.
[29] H. Li, J. Shang, Z. Ai, L. Zhang, *J. Am. Chem. Soc.* **2015**, *137*, 6393–6399.
[30] S. M. S, E. Adabifiroozjaei, Y. Yao, P. Koshy, S. Lim, R. Webster, X. Liu, R. Khayyam Nekouei, C. Cazorla, Z. Liu, Y. Wang, N. Lambropoulos, C. C. Sorrell, *Nat. Commun.* **2019**, *10*, 2594.
[31] H. Idriss, *Surf. Sci.* **2021**, *712*, 121894.
[32] W. J. Kim, D. Pradhan, B.-K. Min, Y. Sohn, *Appl. Catal. B* **2014**, *147*, 711–725.
[33] M. Wang, J. Liu, C. Guo, X. Gao, C. Gong, Y. Wang, B. Liu, X. Li, G. G. Gurzadyan, L. Sun, *J. Mater. Chem. A* **2018**, *6*, 4768–4775.
[34] P. Y.a.T. Byron, *Am. Lab.* **2008**, *40*, 24–27.
[35] M. Mihaylov, K. Chakarova, S. Andonova, N. Drenchev, E. Ivanova, E. A. Pidko, A. Sabetghadam, B. Seoane, J. Gascon, F. Kapteijn, K. Hadjiivanov, *Chem. Commun.* **2016**, *52*, 1494–1497.
[36] Z. Chen, T. F. Jaramillo, T. G. Deutsch, A. Kleiman-Shwarsctein, A. J. Forman, N. Gaillard, R. Garland, K. Takanabe, C. Heske, M. Sunkara, E. W. McFarland, K. Domen, E. L. Miller, J. A. Turner, H. N. Dinh, *J. Mater. Res.* **2011**, *25*, 3–16.
[37] H. Dotan, K. Sivula, M. Grätzel, A. Rothschild, S. C. Warren, *Energy Environ. Sci.* **2011**, *4*, 958–964.
[38] H. Fujito, H. Kunioku, D. Kato, H. Suzuki, M. Higashi, H. Kageyama, R. Abe, *J. Am. Chem. Soc.* **2016**, *138*, 2082–2085.
[39] L. Yu, X. Zhang, G. Li, Y. Cao, Y. Shao, D. Li, *Appl. Catal. B* **2016**, *187*, 301–309.
[40] J. Stephenson, V. Celorrio, D. Tiwari, S. R. Hall, D. C. Green, D. J. Fermín, *J. Electroanal. Chem.* **2018**, *819*, 171–177.
[41] F. A. Harraz, J. Sasano, T. Sakka, Y. H. Ogata, *J. Electrochem. Soc.* **2003**, *150*, C277–C284.
[42] Z. Ran, X. Wang, Y. Li, D. Yang, X.-G. Zhao, K. Biswas, D. J. Singh, L. Zhang, *Npj Comput. Mater.* **2018**, *4*, 14.
[43] Y. Y. Kang, Y. Q. Yang, L. C. Yin, X. D. Kang, L. Z. Wang, G. Liu, H. M. Cheng, *Adv. Mater.* **2016**, *28*, 6471–6477.